Supporting Online Material for

Recycling of Graphite During Himalayan Erosion: A Geological Stabilization of Carbon in the Crust

Valier Galy,* Olivier Beyssac, Christian France-Lanord, Timothy Eglinton

*To whom correspondence should be addressed. E-mail: vgaly@whoi.edu

Published 7 November 2008, *Science* **322**, 943 (2008)
DOI: 10.1126/science.1161408

This PDF file includes:

Materials and Methods
SOM Text
Figs. S1 to S4
Tables S1 and S2
References

Supporting Online Material

Materials and Methods

Sampling of river sediments

River sediments used in this study have been collected during an ongoing effort to document spatial and temporal variability of the sediment load in the Ganges-Brahmaputra river system. In the delta of Bangladesh, in the floodplain (India), as well as at the outflow of the Himalayan range (Nepal), sediments were collected using a "depth sampling" approach (S1, S2). In the delta of Bangladesh depth-sampling was repeated over 4 monsoon seasons (2002, 2004, 2005, 2007). The monsoon season was targeted for sampling because more than 95% of the sediment load is carried within that specific period (S3, S4). The "depth sampling" approach is based on: (1) the collection of suspended sediments along vertical depth profiles from the surface to the bed of the rivers and, (2) the collection by dredging of bed sediments carried at the base of the depth profile. Such a sampling protocol is crucial in order to correctly document sediment heterogeneity in the river section. It allows the integration of this variability and therefore a reliable compositional determination of the overall sediment load. In the Himalayan range, we collected only surface suspended sediments and bed sediments because the depth sampling procedure is impractical in such powerful mountainous rivers (especially during the monsoon). However, it is very likely that sediment heterogeneity is less pronounced in these rivers due to intense re-suspension and mixing of sediments during transport. In any case, surface suspended sediment and bed sediment represent the two extreme end-members and must therefore document sediment heterogeneity in these rivers.

Bengal fan marine sediments

To characterize the Bengal Fan sedimentary system we used sediments collected during the German *R/V Sonne* cruise in February 1994 (S5). In order to account for the spatial heterogeneity in such a large turbiditic system we analysed sediments belonging to its different sub-units (1) the shallow shelf, (2) the channel-levee system of the middle fan and, (3) the distal turbiditic deposits of the lower fan. These sediments were all deposited during the last glacial-interglacial cycle, including recent sediments deposited during the last 500

years (Shelf sediments). Sr and Nd isotopic compositions demonstrate the Himalayan origin of these sediments (S6, S7).

Structural characterization of OC in river and marine sediments

Characterization of the multiscale structural organization (nm to μm) of OC and identification of OC_{petro} has been performed by combining Transmission Electron Microscopy (TEM) and Raman microspectroscopy.

TEM investigations were performed using a JEOL 2010 microscope with an acceleration voltage of 200 kV (UPMC, Paris). Particle size and morphology were imaged with low-magnification mode which also allows selection of particles for high-resolution imaging. The 002 lattice-fringe mode has been used to image directly the profile of the aromatic sheets, and thus to have some insight into the structure of the aromatic skeleton including extent of graphitic layers (in plane and stacking), porosity and heterogeneity (S8 and references therein). This high-resolution mode was coupled with selected area electron diffraction (SAED) to detect the presence of triperiodic graphite *sensu stricto* (see Fig. S3). TEM investigations were performed on OC isolated from the sediments. Sediments were first ground and then submitted to HCl/HF acid attack to eliminate carbonates and silicates phases. Thermal treatment to accelerate acid attacks never exceeded ~70°C to avoid any artefact transformation of OC_{petro} during sample preparation. Sample residues after acid digestion were ground in an agate mortar, dispersed by ultrasounds in anhydrous ethanol and finally deposited on TEM grids covered by a holey amorphous carbon film. Observations were performed on the thinnest fragments placed across the holes.

Raman microspectroscopy was performed using a Renishaw InVia system (ENS, Paris). We used a 514.5 nm Ar Spectra Physics laser, an 1800 grooves/mm holographic grating to disperse the backscattering signal and a RenCam CCD detector for analysis; the system is also equipped with a XYZ Prior motorized stage for mapping. The laser was focussed on the sample through a Leica DMLM microscope with x50 long-working (Numerical Aperture 0.50) and short-working (Numerical Aperture 0.75) distance objectives. In such configuration, the laser spot size is ~2 μm in diameter at sample surface, and we selected a low laser power at sample surface of ~1 mW to avoid any sample transformation due to laser-induced heating (S9 and references therein). The spectrometer was calibrated for every session with a Neon lamp and/or a silicon wafer. Using the synchroscan mode from 100 to 2000 cm^{-1}, Raman modes of both (i) silicates/carbonates minerals (100-1100cm^{-1}) as well

as (ii) graphitic carbonaceous material (1300-1600 cm^{-1}) were recorded simultaneously. Raman analyses were performed directly on the raw powder recovered from suspended and bed loads in rivers and from marine sediments. No sample preparation is needed for such Raman analysis thus preserving physical relationships between OC and minerals. Recording a Raman spectrum requires less than a minute, so hundreds of particles were checked using Raman microspectroscopy, either in mapping or manual mode, to have an insight into the sample heterogeneity. The first-order Raman spectrum of graphitic C is composed of (1) a main graphite G band at ~1580 cm^{-1} (in-plane stretching mode of aromatic C) and (2) several defect bands at 1350, 1500 and 1600 cm^{-1} which correspond to physico-chemical defects in the graphitic structure (S9). In pristine graphite only the G band is observed, whereas in polycrystalline graphite and/or disordered graphitic C, G as well as defects bands are present. The relative intensity of the defect bands compared to the G band is a sensitive quantitative marker of the degree of graphitization and has been extensively used in materials (S10) and Earth (S11) sciences.

Determination of OC content and radiocarbon composition.

OC content and radiocarbon composition were determined after decarbonation of the bulk sediments, following the procedure described in (S12). The solubilization of a fraction of the OC during this procedure was accounted for in order to obtain actual total OC content (S12). ^{14}C measurements were performed on both LMC14 (Gif sur Yvette) and NOSAMS (Woods Hole) national accelerator mass spectrometery (AMS) facilities. The results are expressed as fraction of modern C (Fm), defined as the ratio between (1) ^{14}C activity of the sample and, (2) 95% of the ^{14}C activity of the oxalic acid standard (S13). A correction for $^{13}C/^{12}C$ variations was applied and all the results were normalised to a $\delta^{13}C$ of -25‰. The overall uncertainty associated with total OC content and ^{14}C composition determination is presented for each sample in table S2.

Supporting online text

On the origin of graphitic OC in river and marine sediments

In many recent publications, a refractory OC pool, chemically and physically resistant, was identified in river and marine sediments (S14-16) as well as in soils (S17-19); this pool is often referred to as graphitic black carbon (S20, S21). GBC are the best candidate for the origin of the ^{14}C depleted OC pool, often referred to as fossil OC, which has been observed in various sedimentary contexts (S1, S15, S22, S23).

In these studies, however, GBC may include authentic OC_{petro} or combustion products (soots, charcoals). It may also be an artefact, generated by thermal treatment of OC during sample preparation, for instance during HF/HCl treatments at high temperature (T>300°C) as suggested by Haberstroh et al. (S16). Here our extraction procedure with a maximal temperature of 70°C should avoid any inadvertent synthesis of GBC. The key remaining question is how to ascribe a petrogenic origin to graphitic phases rather than other possible (pyrogenic) origins. The aromatic skeleton of OC_{petro} as imaged by TEM, is much more developed in petrogenic C than in any combustion products: in 002 lattice fringes images, the in-plane extent as well as the number of stacked layers of coherent domains is much higher in petrogenic OC. For instance, 002 lattice-fringes images of charcoal, soots, refractory OC in sediments or soils (S18, S19) are completely different from images obtained from C extracted from metamorphic rocks including coals (S8, S24). Most of the graphitic phases observed in this study in both river and marine sediments exhibit a well developed aromatic structure very similar to that of petrogenic C, as also suggested by SAED observations (Figure S3).

This is confirmed by Raman microspectroscopy investigations, which were performed on selected particles identified as possibly petrogenic on the basis of textural habit under the microscope and avoiding recent OC fragments. First, all the graphitic phases for which the Raman spectrum shows a mineral contribution and which are intimately associated with minerals (inclusions, aggregates) as observed under the microscope have unambiguously a petrogenic origin. More generally, the Raman spectra obtained from a large fraction of graphitic C are very similar to those obtained from petrogenic C in metamorphic rocks (S11), in particular from the Lesser Himalaya and High-Himalayan Crystalline (S25) in terms of relative intensity of defect bands to the graphite G band. Some of the spectra from the most disordered graphitic phases and obtained on isolated particles are actually comparable to spectra from soots (S26) or charcoals (S27, S28). Such spectra which might correspond either

to non petrogenic phases or to a sedimentary origin of C were not considered as representative of OC_{petro}.

The presence in river sediments of highly disordered carbonaceous phases derived from rock erosion cannot be ruled out. However, in the Himalayan system, the vast majority of petrogenic C derives from the series from the mountain belt (mostly High Himalaya Crystalline and Lesser Himalaya and to a lower extent Tethyan Sedimentary Series), which are all metamorphosed rocks in which petrogenic C is properly detectable using RM and TEM.

The use of bulk ^{14}C data to calculate the content of rock-derived OC in river sediments

The particulate organic carbon exported by rivers can be described as a mix between a "rock-derived" component and a "non rock-derived" component. The former pool of OC represents any organic carbon particle that was initially contained in source rocks of the catchment. They can be liberated during physical erosion and/or remain included in minerals and rock fragments transported by the rivers. In the following discussion we design this pool by the generic appellation OC_{petro}. The second end-member represents all other particles of OC, i.e. those which have never been contained in rocks. This latter pool is actually mostly composed of a vegetation component (fresh plant litter + degradation products or detritus), a soil component, and particulate material derived from autotrophy within the river. In the following discussion we define the non rock-derived pool by the generic appellation OC_{recent}. Hence, the measured radiocarbon composition of each river sediment can be expressed by the following binary mixing equation:

$$Fm = \frac{\%OC_{petro}}{\%OC} \times Fm_{OCpetro} + \frac{\%OC_{recent}}{\%OC} \times Fm_{OCreccent} \quad (1)$$

where:

Fm is the measured radiocarbon composition of the sample expressed as the fraction of modern C (S13),

$\%OC_{petro}$ is the concentration of petrogenic OC in the sample (expressed as % of dry weight),

$\%OC_{recent}$ is the concentration of recent OC in the sample (expressed as % of dry weight),

%OC is the total concentration of OC in the sample (expressed as % of dry weight),

$Fm_{OCpetro}$ is the radiocarbon composition of the petrogenic OC,

$Fm_{OCrecent}$ is the radiocarbon composition of the recent OC in the sample.

In this model, a first assumption is that the radiocarbon composition of the rock-derived component is $Fm_{OCpetro} = 0$. This actually means that rock-derived OC has a radiocarbon activity lower than the detection limit of the AMS used for the measurement, or more explicitly, that the age of OC_{recent} is older than ca. 60 ka. This is obviously the case in the Himalayan system where any rock exposed at the surface (i.e. submitted to erosion) is much older than 60 ka.

The second assumption is that the upper limit of the probability density of the age of the $OC_{rencent}$ is 60 ka. In other words, we posit that the non rock-derived component is devoid of particles older that 60 ka. In the Himalayan system, surface soils contain the oldest component of OC_{recent} and have a residence time much lower than 60 ka. The binary mixing model of the radiocarbon composition is therefore valid.

Consequently, equation (1) can be simplified by injecting $Fm_{OCpetro} = 0$:

$$Fm = \frac{\%OC_{recent}}{\%OC} \times Fm_{OCrecent} \quad (2)$$

Multiplying both terms of the equation by %OC, we can rewrite the equation as follows:

$$\%OC \times Fm = \%OC_{recent} \times Fm_{OCrecent} \quad (3)$$

A corollary of the binary mixing model is that total OC content of each sediment sample must be the sum of its OC_{petro} and OC_{recent} content:

$$\%OC = \%OC_{petro} + \%OC_{recent} \quad (4)$$

Equation (4) can be rearranged to express $\%OC_{recent}$:

$$\%OC_{recent} = \%OC - \%OC_{petro} \quad (5)$$

Finally, inserting equation (5) in equation (3) lead to the following expression:

$$\%OC \times Fm = \%OC \times Fm_{OCrecent} - \%OC_{petro} \times Fm_{OCrecent} \quad (6)$$

Operating the variable replacement Y = %OC×Fm and X = %OC, equation (6) can be rewritten as:

$$Y = Fm_{OCrecent} \times X - (\%OC_{petro} \times Fm_{OCrecent}) \quad (7)$$

Consequently, every sample plotting on a straight line in a diagram representing the product %OC×Fm (Y) as a function of %OC (X) are characterized by similar $\%OC_{petro}$. In this case, the OC_{petro} content can be simply determined as the intersect between the trend and the X axis (the X value for Y=0).

In the Ganges-Brahmaputra system, river sediments collected along depth profiles statistically define linear trends in such a diagram (see figures 2 and S3). Thus, sediments belonging to the same depth profile have similar $\%OC_{petro}$, which can thus be determined using a statistical analysis of their linear regression. The results are presented in table S2. Regarding their major element composition, sediments collected along a depth profile can be interpreted as a binary mixing between bed sediment and a fine grained, aluminous rich end-member. Thus, since (1) bed sediments almost exclusively contain OC_{petro} and, (2) the aluminous end-member has a unique composition for each depth sampling, then the geochemical binary mixing produces a set of sediments characterized by a unique $\%OC_{petro}$ value. The use of sediments collected along depth profiles is therefore a key to unravel the mixture of rock-derived and recent OC in rivers.

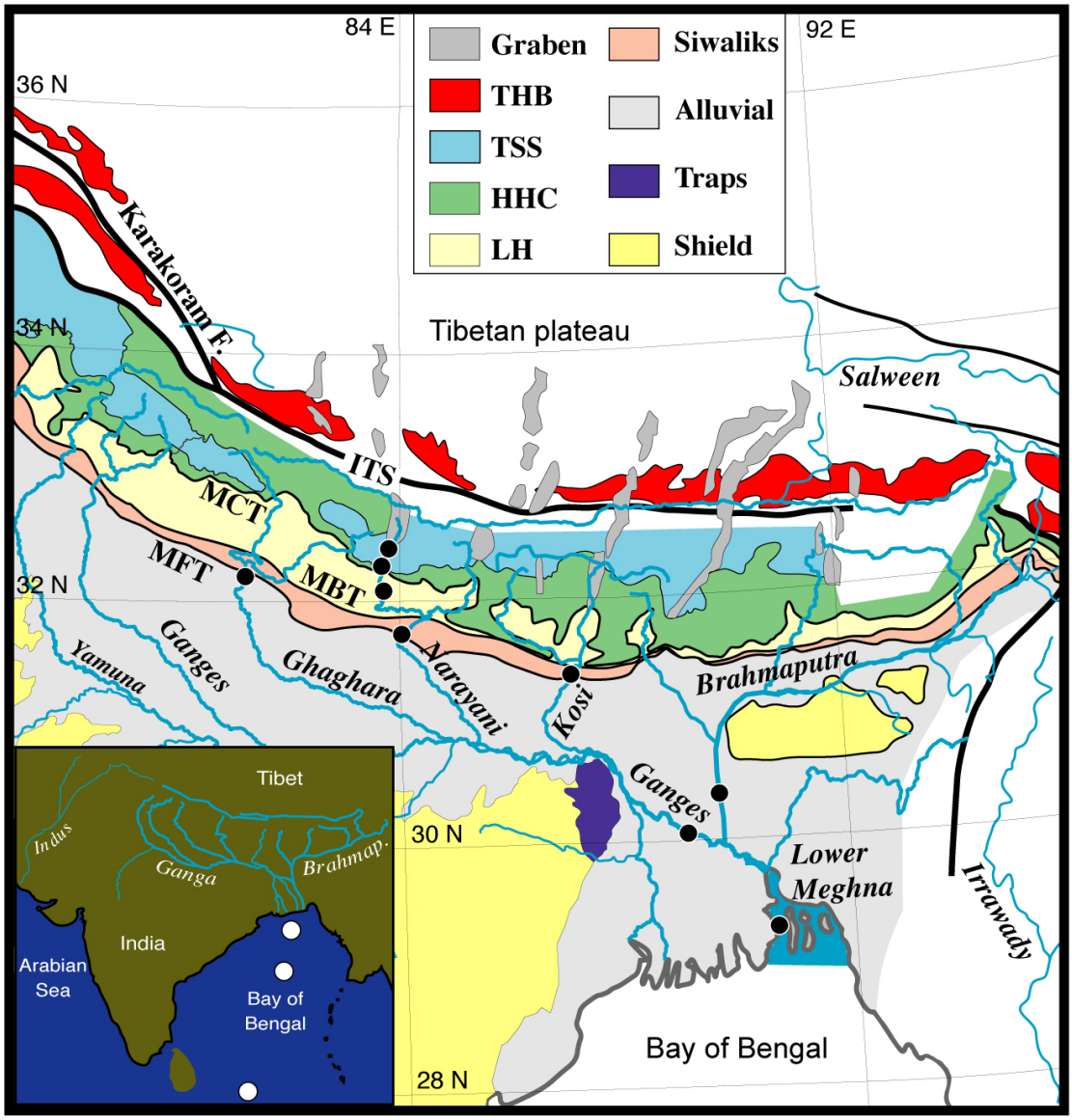

Figure S1: Simplified geological map of the Himalayan system showing the Ganges-Brahmaputra river system and the location of sampling sites used in this study (black dots). The four major lithologic units of the Himalayan range are represented; THB = Trans-Himalayan batholiths, TSS = Tethyan Sedimentary Series, HHC = High Himalaya Crystalline, LH = Lesser Himalaya. HHC and upper LH are high-grade metamorphism series while TSS, lower LH and Siwaliks are low-grade metamorphism series. Major structural features are also shown; ITS = Indus-Tzangpo Suture, MCT = Main Central Thrust, MBT = Main Boundary Thrust, MFT = Main Frontal Thrust. The three main tributaries of the Ganges were sampled at the outflow of the Himalayan range, i.e. close to the transition between the Siwaliks (composed of re-exhumed Mio-Pliocene Himalayan sediments) and the Indo-Gangetic floodplain composed of Quaternary fluvial deposits. Ganges, Brahmaputra and Lower Meghna have been sampled in the delta of Bangladesh.

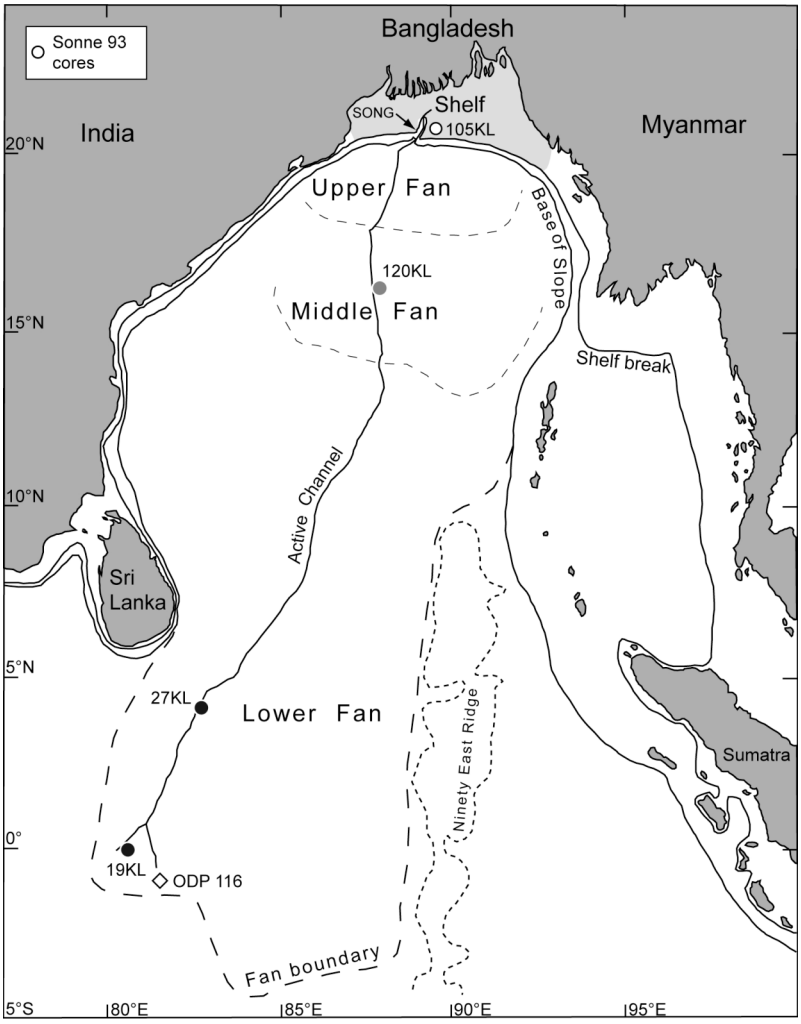

Figure S2: Map of the Bengal fan turbiditic system showing the location of the cores used in this study. To describe the main sub-units of the fan Short, we analysed sediments from piston cores drilled by the R/V Sonne in February 1994 (Sonne 93 cruise).

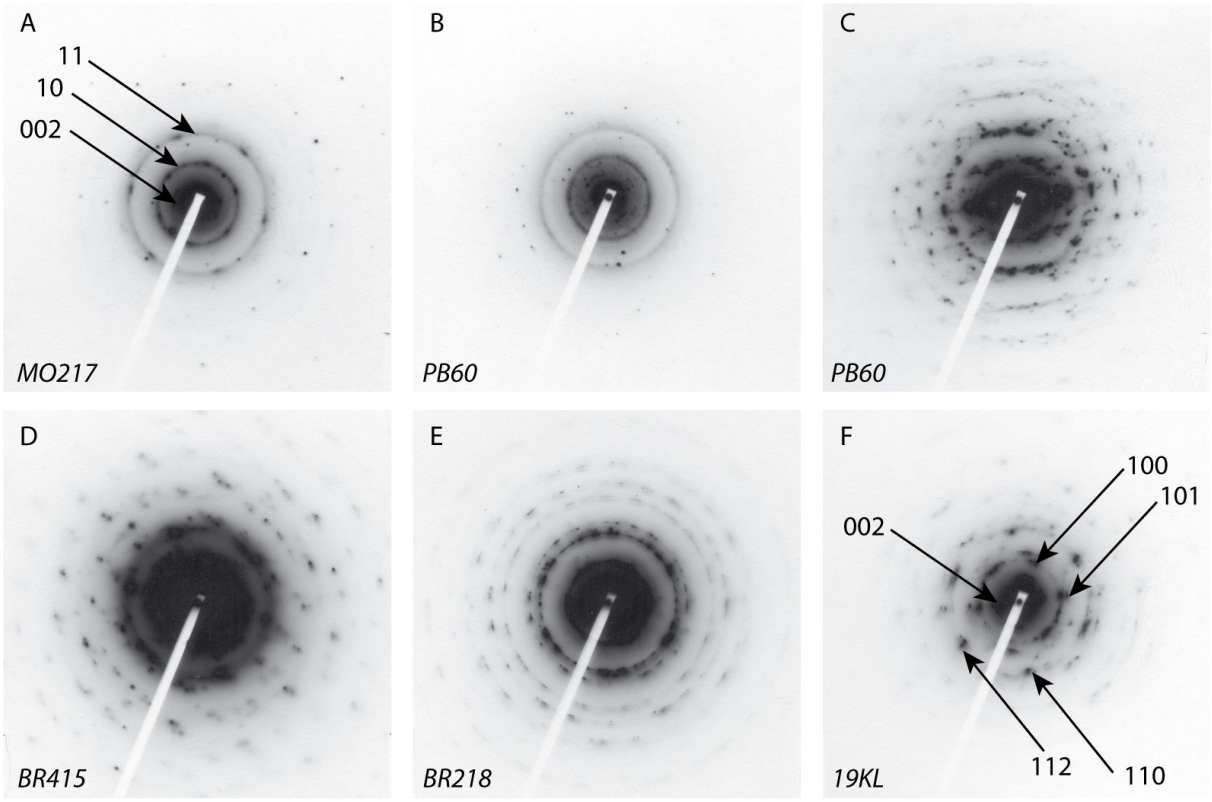

Figure S3: Representative selective area electron diffraction (SAED) patterns of graphitic OC obtained in river and marine sediments. Owing to the aperture used, these SAED patterns were sampled on a surface of ~1-2 μm^2. (A): disordered and heterogeneous OC_{petro} in Narayani suspended load sediment. This SAED pattern corresponds to a mixture of graphitic OC_{petro} (punctuation of 002 and *hk* bands) and turbostratic OC_{petro} (continuous rings for 002 and *hk* bands). (B): disordered and heterogeneous OC_{petro} in Narayani bed load sediment. (C): polycrystalline graphite in Narayani bed load sediment. (D): polycrystalline graphite in Ganges suspended load sediment. (E): polycrystalline graphite in Lower Meghna suspended load sediment. (F): polycrystalline graphite in distal Bengal fan sediment. In this SAED pattern, both the presence of *hk* bands punctuation and modulation of 11. bands (110 and 112 reflections) indicate the presence of graphite micro-crystallites. See (S8) for further discussion on SAED of graphitic C.

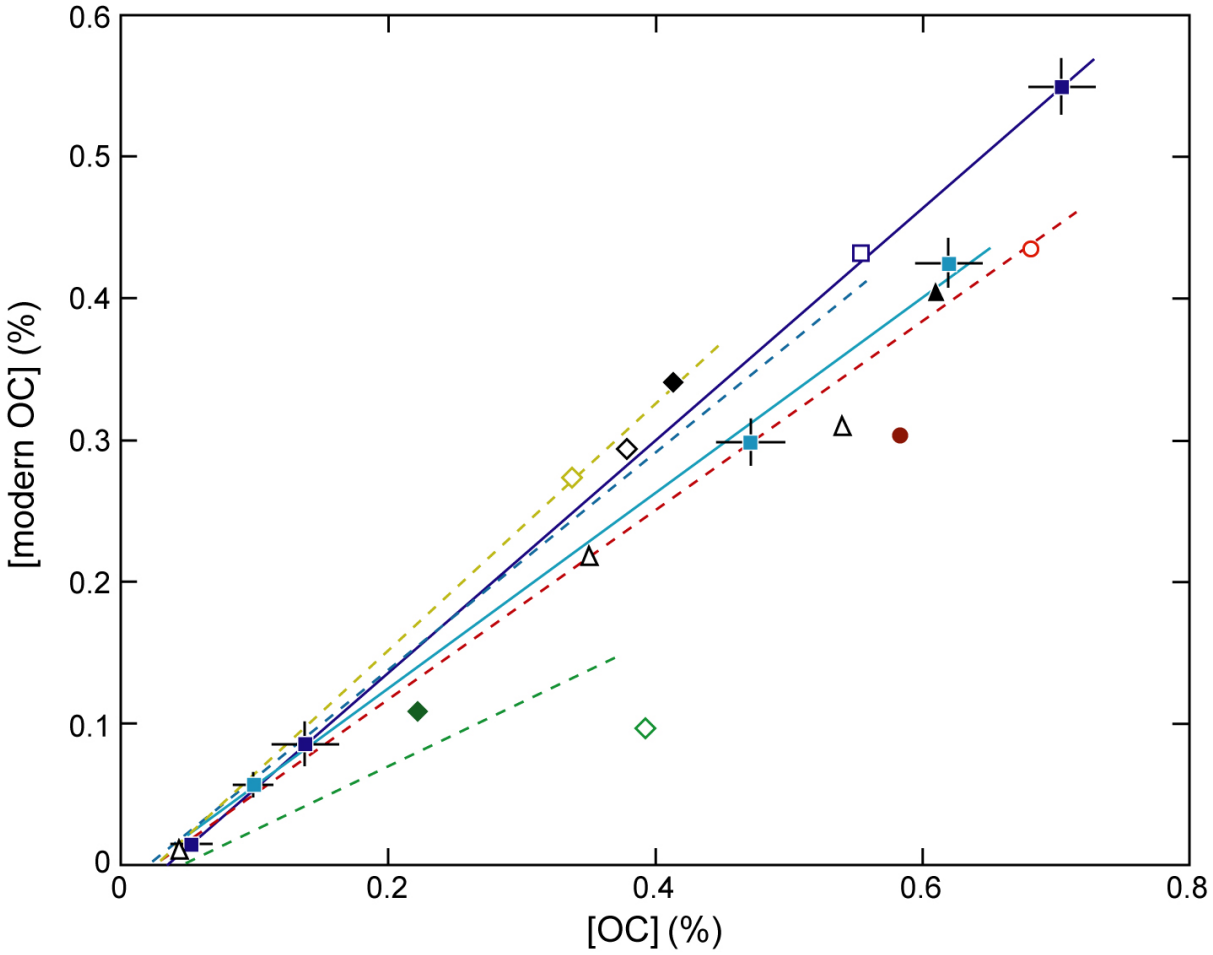

Figure S4: Modern OC content (Fm × % OC) of sediments collected over depth profiles in rivers from the G-B system as a function of their total OC content.. The dashed lines reflect the best fit obtained for depth sampling sets presented in figure 2. Two additional depth sampling sets of the Ganges in Bangladesh are presented (light blue squares = 2002, dark blue squares = 2005) together with their best linear fits (solid lines). The variability between the 3 depth sampling sequences of the Ganges in Bangladesh is mostly related to different composition of the OC_{recent}, since the three trends converge towards a similar $\%OC_{petro}$ value. The composition of surface suspended load sampled in 2007 are also reported (Ganges = open blue square, Brahmaputra = open red dot, Lower Meghna = black triangle, Kosi = open yellow diamond, Karnali = open black diamond, Narayani = open green diamond) as well as additional data for the Lower Meghna (open triangles), the Karnali (black diamond), the Narayani (green diamond) and the Brahmaputra (red dot). Although these data do not allow the calculation of $\%OC_{petro}$, they mostly confirm those obtained for depth sampling sets. The Narayani appears to exhibit the greatest heterogeneity, which may be attributed to variable proportions of old organic carbon derived from Northern part of the catchments. In contrast, Kosi and Karnali seem to have more stable composition throughout time.

Table S1: Characteristics of the samples analysed by Raman micro-spectroscopy (Ra.) and Transmitted Electron Microscopy (TEM)

Sample #	Basin	Location	Date	Type	Analysis
MO 501	Kali Gandaki	Tukuche		SL 0m	Ra.
NAG 38		Dana		BL	Ra.
PB 29		Tatopani	8/07/05	BL	Ra. + TEM
PB 31				SL 0m	Ra. + TEM
MO 217	Narayani	Narayanghat	20/05/97	BL	Ra. + TEM
PB 60			11/07/05	SL 0m	Ra. + TEM
BR 415	Ganges	Harding Bridge	13/07/04	SL 0m	Ra. + TEM
BR 411				SL 9m	Ra.
BR 418				BL	Ra. + TEM
BR 522			23/07/05	SL 0m	Ra.
BR 451	Brahmaputra	Sirajganj	23/07/04	BL	Ra.
BR 457				SL 0m	Ra. + TEM
BR 456				SL 3m	Ra.
BR 455				SL 6m	Ra.
BR 460				BL	Ra. + TEM
BR 218	Lower Meghna	Bohla	18/07/02	SL 0m	Ra. + TEM
BR 216				SL 10m	Ra.
BR 219				BL	Ra. + TEM
BR 440			18/07/04	SL 6m	Ra.
105KL 77-86	Bengal Fan	Shelf		marine sed.	Ra. + TEM
105KL 758-765				marine sed.	Ra. + TEM
120KL 1030-1031		Channel-levee		marine sed.	Ra. + TEM
120KL 1114-1117				marine sed.	Ra.
27KL 630-631		Distal Fan		marine sed.	Ra. + TEM
19KL 153-155				marine sed.	Ra. + TEM

SL = suspended load (with depth of sampling), BL = bed load, marine sed. = marine sediment

Table S2: Radiocarbon composition (Fm) of river sediments from the G-B system and calculated content of OC_{petro} for sediments collected along depth profiles.

Sample #	Basin	Location	Type	date	Fm	σ(Fm)	OC (wt %)	σ(OC)	OC*Fm	σ(OC*Fm)	OC_{petro} (wt %)	Probability of fit (2σ)
PB 68	Kosi	Chatara	SL 0m	15/07/05	0.81	0.006	0.42	0.025	0.34	0.021	0.027	0.58
PB 69[§]			SL 0m		0.84	0.006	0.35	0.025	0.29	0.021		
PB 65			SL 3.8m		0.77	0.005	0.32	0.025	0.25	0.019		
PB 70			BL		0.39	0.005	0.05	0.015	0.02	0.010		
LO 765[§]			SL 0m	10/08/07	0.81	0.004	0.34	0.025	0.27	0.020		
MO 331	Narayani	Narayanghat	SL 0m	10/07/98	0.49	0.003	0.22	0.025	0.11	0.012		
PB 60			SL 0m	11/07/05	0.39	0.006	0.34	0.025	0.13	0.010	0.046	0.89
PB 58			SL 0m		0.39	0.006	0.33	0.025	0.13	0.010		
PB 56			SL 4m		0.37	0.004	0.21	0.025	0.08	0.009		
PB 54			SL 8m		0.33	0.004	0.18	0.025	0.06	0.008		
LO 742[§]			SL 0m	8/08/07	0.31	0.002	0.39	0.025	0.10	0.008		
PB 79	Karnali	Chisapani	SL 0m	15/07/05	0.83	0.005	0.41	0.025	0.34	0.021		
LO 753[§]		Kotillaghat	SL 0m	10/08/07	0.78	0.004	0.38	0.025	0.29	0.019		
BR 208*	Ganges	Harding Bridge	SL 10m	15/07/02	0.68	0.003	0.62	0.025	0.42	0.017	0.021	0.15
BR 210*			SL 17m		0.63	0.003	0.47	0.025	0.30	0.016		
BR 214*			BL 22m		0.56	0.004	0.10	0.015	0.06	0.008		
BR 415*			SL 0m	13/07/04	0.74	0.003	0.53	0.025	0.39	0.018	0.021	0.94
BR 414*			SL 2m		0.74	0.005	0.46	0.025	0.34	0.019		
BR 413*			SL 4m		0.71	0.005	0.42	0.025	0.30	0.018		
BR 411*			SL 9m		0.70	0.003	0.22	0.025	0.16	0.018		
BR 418*			BL 10m		0.18	0.003	0.03	0.015	0.01	0.003		
BR 522*			SL 0m	23/07/05	0.78	0.003	0.70	0.025	0.55	0.020	0.035	0.90
BR 520[§]			BL 10m		0.62	0.003	0.15	0.025	0.09	0.015		
BR 516*			BL 11m		0.29	0.004	0.05	0.015	0.02	0.004		
BR 711[§]			SL 0m	17/08/07	0.78	0.004	0.55	0.015	0.43	0.012		
BR 457*	Brahmaputra	Sirajganj	SL 0m	23/07/04	0.66	0.004	0.69	0.025	0.45	0.017	0.028	0.47
BR 456*			SL 3m		0.60	0.008	0.45	0.025	0.27	0.015		
BR 454*			SL 9m		0.57	0.003	0.29	0.025	0.16	0.014		
BR 453[§]			BL		0.58	0.003	0.19	0.015	0.11	0.009		
BR 460*			BL 10m		0.23	0.002	0.04	0.015	0.01	0.003		
BR 500*			SL 0m	21/07/05	0.52	0.003	0.58	0.025	0.30	0.013		
BR 709[§]		Jamuna bridge	SL 0m	16/08/07	0.64	0.003	0.68	0.015	0.44	0.010		
BR 444*	L Meghna	Bohla	SL 2m	18/07/04	0.58	n.d.	0.54	0.025	0.31	n.a.		
BR 439*			SL 8m		0.63	n.d.	0.35	0.025	0.22	n.a.		
BR 446*			BL 11m		0.29	n.d.	0.04	0.015	0.01	n.a.		
BR 720[§]		Mawa	SL 0m	19/08/07	0.66	0.003	0.61	0.015	0.41	0.010		
120KL 141	Bengal fan	Channel-levee	sediment		0.71	0.004	0.73	0.025	0.52	0.018		
120KL 850			sediment		0.75	0.005	0.71	0.025	0.54	0.019		

The radiocarbon composition of river sediment is expressed as the Fraction of modern C (Fm). Total organic carbon content (OC) is expressed as weight % of dry sediment. Associated uncertainty are given for each measurement (σ(Fm), σ(OC)) as well as calculated uncertainty on the amount of modern OC (σ(Fm*OC)). For sediments collected along depth profiles, calculated content of OC_{petro} are indicated. The probability that depth sampling sets define a linear trend (at 2σ) is also given.

SL = suspended load (with depth of sampling), BL = bed load, n.d. = not determined, n.a. = not applicable, * indicate data from *(S1),* [§] indicate sediments analysed at NOSAMS.

References

S1. V. Galy *et al.*, Nature 450, 407 (2007).
S2. V. Galy, C. France-Lanord, B. Lartiges, Geochimica et Cosmochimica Acta 72, 1767 (2008).
S3. G. M. T. Islam, S. T. Jaman, Water Management 159, 87 (2006).
S4. RSP, "Spatial representation and analysis of hydraulic and morphological data" Tech. Report No. FAP 24 (Water Resources Planning Organization (WARPO), 1996).
S5. H. Kudrass, "Bengal Fan, Sonne cruise 93" (BGR, 1996).
S6. A.-C. Pierson-Wickmann, L. Reisberg, C. France-Lanord, H. Kudrass, Paleoceanography 16, 435 (2001).
S7. V. Galy *et al.*, Quaternary Science Reviews 27, 1396 (2008).
S8. O. Beyssac, J.-N. Rouzaud, B. Goffé, F. Brunet, C. Chopin, Contributions to Mineralogy and Petrology 143, 19 (2002).
S9. O. Beyssac *et al.*, Spectrochimica Acta Part A 59, 2267 (2003).
S10. A. C. Ferrari, J. Robertson, Physical Review B 61, 14095 (2000).
S11. O. Beyssac, B. Goffé, C. Chopin, J.-N. Rouzaud, Journal of metamorphic geology 20, 859 (2002).
S12. V. Galy, J. Bouchez, C. France-Lanord, Geostandards and Geoanalytical research 31, 199 (2007).
S13. W. G. Mook, J. Van der Plicht, Radiocarbon 41, 227 (1999).
S14. A. F. Dickens *et al.*, Geochimica et Cosmochimica Acta 70, 666 (2006).
S15. A. F. Dickens, Y. Gélinas, C. A. Masiello, S. Wakeham, J. I. Hedges, Nature 427, 336 (22/01/2004, 2004).
S16. P. R. Haberstroh *et al.*, Geochimica et Cosmochimica Acta 70, 1483 (2006).
S17. J. Lehmann *et al.*, Global Biogeochemical Cycles 19 (2005).
S18. N. Poirier *et al.*, Organic Geochemistry 31, 813 (2000).
S19. M. W. I. Schmidt, J. O. Skjemstad, C. Jager, Global Biogeochemical Cycles 16 (2002).
S20. E. R. M. Druffel, Marine Chemistry 92, 197 (2004).
S21. C. A. Masiello, Marine Chemistry 92, 201 (2004).
S22. N. E. Blair *et al.*, Geochimica et Cosmochimica Acta 67, 63 (2003).
S23. C. A. Masiello, E. R. M. Druffel, Geophysical Research Letters 30 (2003).
S24. P. R. Buseck, B.-J. Huang, Geochimica et Cosmochimica Acta 49, 2003 (1985).
S25. O. Beyssac, L. Bollinger, J.-P. Avouac, B. Goffe, Earth and Planetary Science Letters 225, 233 (2004).
S26. A. Sadezky, H. Muckenhuber, H. Grothe, R. Niessner, U. Pˆschl, Carbon 43, 1731 (2005).
S27. D. Alon, G. Mintz, I. Cohen, S. Weiner, E. Boaretto, Radiocarbon 44, 1 (2002).
S28. K. Ishimaru, T. Hata, P. Bronsveld, D. Meier, Y. Imamura, Journal of Materials Science 42, 122 (2007).